Influence of picosecond multiple/single line ablation on copper nanoparticles fabricated for surface enhanced Raman spectroscopy and photonics applications

2013 J. Phys. D: Appl. Phys. 46 485501

(http://iopscience.iop.org/0022-3727/46/48/485501)

J. Phys. D: Appl. Phys. **46** (2013) 485501 (14pp) doi:10.1088/0022-3727/46/48/485501

Influence of picosecond multiple/single line ablation on copper nanoparticles fabricated for surface enhanced Raman spectroscopy and photonics applications

Syed Hamad[1], **G Krishna Podagatlapalli**[2], **Surya P Tewari**[1,2] **and S Venugopal Rao**[2]

[1] School of Physics, University of Hyderabad, Prof. C.R. Rao Road, Hyderabad 500046, India
[2] Advanced Center of Research in High Energy Materials (ACRHEM) University of Hyderabad, Prof. C.R. Rao Road, Hyderabad 500046, India

E-mail: soma_venu@yahoo.com or svrsp@uohyd.ernet.in

Received 18 July 2013, in final form 1 October 2013
Published 7 November 2013
Online at stacks.iop.org/JPhysD/46/485501

Abstract
A comprehensive study comprising fabrication of copper nanoparticles (NPs) using picosecond (ps) multiple/single line ablation in various solvents such as acetone, dichloromethane (DCM), acetonitrile (ACN) and chloroform followed by optical, nonlinear optical (NLO), and surface enhanced Raman spectroscopy (SERS) characterization was performed. The influence of surrounding liquid media and the writing conditions resulted in fabrication of Cu NPs in acetone, CuCl NPs in DCM, CuO NPs in ACN and $CuCl_2$ NPs in chloroform. Prepared colloids were characterized through transmission electron microscopy, energy dispersive x-ray spectra, selected area electron diffraction and UV-visible absorption spectra. A detailed investigation of the surface enhanced Raman scattering (SERS) activity and the ps NLO properties of the colloids prepared through multiple/single line ablation techniques revealed that the best performance was achieved by Cu NPs for SERS applications and $CuCl_2$ NPs for NLO applications.

(Some figures may appear in colour only in the online journal)

1. Introduction

In the present scenario of advances in science and technology, metal/metal oxide nanoparticles (NPs) have received a great deal of attention due to their potential applications in the fields of biomedicine, photonics, and surface enhanced Raman spectroscopy (SERS) [1–6]. The dramatic behaviour of metallic nano-entities is attributed to the modification of electronic eigenstates, subject to diverse boundary conditions in the nano-scale, leading to unique electronic, optical, magnetic, and mechanical properties. The spectacular characteristics of nanomaterials, mediated by localized surface plasmon resonances (LSPR), have been successfully exploited in the fields of spectroscopy, medicine, and photonics. Colloidal metal NPs are advantageous compared to other SERS active substrates since the Raman spectrum from a metal colloid is resultant from the signal average of the individual metal NPs in a colloidal suspension [7]. Laser ablation in liquid media [8–20] is a rapid and simple technique to fabricate NPs because of inhibited multistep chemical synthesis, long reaction times, and high bulk temperatures. Ultrafast laser ablation (ULA) of metallic target in liquid [21–27] guarantees extremely stable NPs without using chemical precursors with a highest degree of safety since fabricated NPs are in colloidal form rather than powders (hence, free of inhalation accidents).

Unlike ablation with nanosecond (ns) laser pulses, ULA [28, 29] is free from transient interference with the produced metallic plume. The ablation threshold in this regime becomes independent of the pulse duration [30–32]. The rate of fabrication of Cu NPs in picosecond (ps) domain

was established to be 3–4 times faster than in the fs domain [33, 34]. Additionally, the induction of nonlinear effects, resulting from solvents, in ps regime is negligible compared to the fs regime. Thus far, people have reported the influence of surrounding liquid media in determination of yield and size distribution of NPs. In the present work, emphasis was on the fabrication of copper NPs via multiple and single line ablation conditions and the interim interaction of transient metallic plume with the surrounding liquid environment. The intrinsic nature of liquid medium and writing conditions resulting in fabrication of different NPs, such as Cu, CuCl, CuO and $CuCl_2$ were observed. The outcome of the ablation was observed to end up with Cu NPs of different nature exclusively depending on the properties of the chosen liquid media. Herein, we have extensively investigated and discussed (a) the influence of multiple/single line ablation on fabrication of Cu NPs of different morphologies and the effect of surrounding medium (b) Raman studies of Copper NPs obtained using ablation in different liquids (c) dependence of nonlinear optical (NLO) properties of the NPs on different writing conditions (multiple/single line ablation).

2. Experimental details

2.1. Method of preparation

Four organic solvents namely acetone, dichloromethane (DCM), acetonitrile (ACN) and chloroform were used for fabrication of NPs and multiple/single line ablation was performed by a Ti : sapphire laser system (LEGEND, Coherent) delivering nearly bandwidth limited laser pulses (∼2 ps, 1 kHz repetition rate) at 800 nm. The amplifier was seeded with ∼15 fs (55–60 nm FWHM) pulses from an oscillator (MICRA, Coherent, 750 mW, 76 MHz, 800 nm). Pure Cu targets were washed with Acetone after sonication to eliminate any residual organic impurities from the surface. The target was placed into a Pyrex cell and covered by a layer of absolute liquids. After ensuring the substrate was perfectly parallel to optical bench, laser pulses were allowed to focus onto the Cu substrate using a plano-convex lens ($f = 25$ cm). It is crucial to adjust the focus exactly on the surface of metal substrate immersed in liquid since the refractive index of the liquid medium modifies the focal position resulting in poor fabrication rate [35–37]. The beam diameter ($2\omega_0$) estimated at the focus in air was ∼40 μm. The typical level of liquid above the metal surface was ∼7 mm. The experimental schematic of the ps laser ablation is illustrated in figure 1(*a*).

Exact beam waist on the Cu strip immersed in liquid media was estimated as the method proposed by Menendez-Manjon *et al* [37]. Initially, a rough estimate of correction to the focal plane (Δf) was achieved through consideration of the refractive index of liquid (level also) in which the ablation was performed. Later on, sample position was changed with respect to the correction of Δf. Cu targets were placed normal to incident laser beam on a motorized X–Y stage, which was operated through a motion controller (Newport ESP 300). Typical fluence used was ∼8 J cm^{-2}. The scanning speeds of X–Y stages were 0.1 mm s^{-1} in each

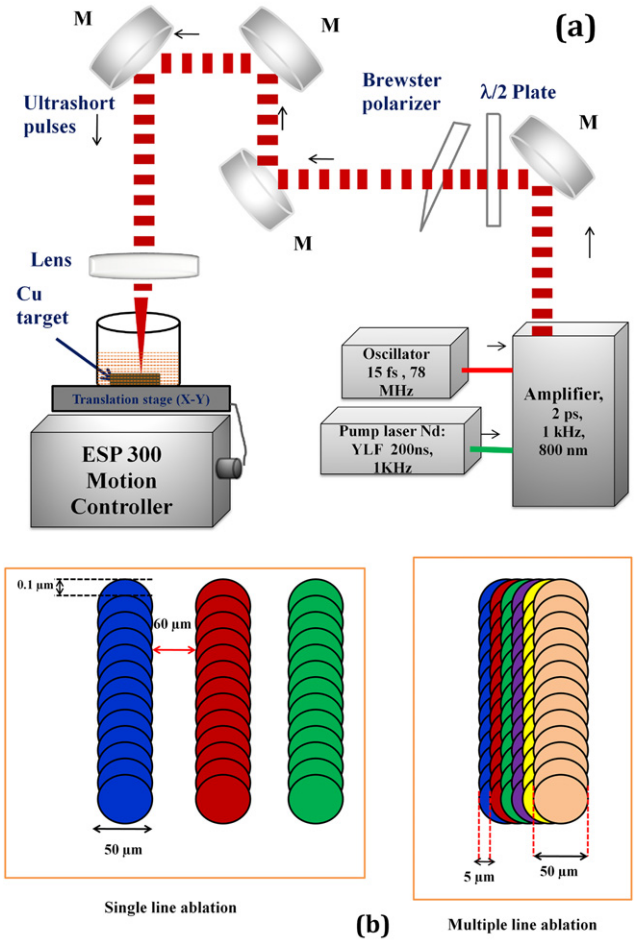

Figure 1. (*a*) Schematic of the ps laser ablation experimental setup (*b*) schematic of the pulses incident on target.

direction. The motorized stages were scanned in such a way as to draw periodic lines on the surface with the given spacing of (a) ∼60 μm and (b) ∼5 μm. Based on the scanning configuration, two types of ablation were carried out: (a) single line ablation wherein the average number of pulses incident per spot on the target was ∼500 (0.1 μm ms^{-1} speed, 1 pulse ms^{-1} and assuming a spot diameter of ∼50 μm on the target in liquid). Figure 1(*b*) shows the schematic of the scanning and the pulses' impact on the target; (b) multiple line ablation wherein line structures were overlapped. The ablation in this regime is slightly complicated since the spot diameter ($2\omega_0$) was ∼50 μm on the substrate and the line separation was ∼5 μm. The average number of pulses incident per spot on the target were ∼4000. We expect a gradient in the number of pulses incident (perpendicular to the scan direction) and consequently the ablation could be inhomogeneous. In the second case scan separation exceeded the dimensions of beam waist on the surface and, therefore, line structures drawn by the laser were distinguishable since they were separated from one another, which was confirmed from images obtained by optical microscope. To avoid the ambiguity, Cu NPs prepared through multiple line (single line) ablation in acetone, DCM, ACN, and chloroform are labelled as MCuNP1 (SCuNP1), MCuNP2 (SCuNP2), MCuNP3 (SCuNP3), and MCuNP4 (SCuNP4), respectively.

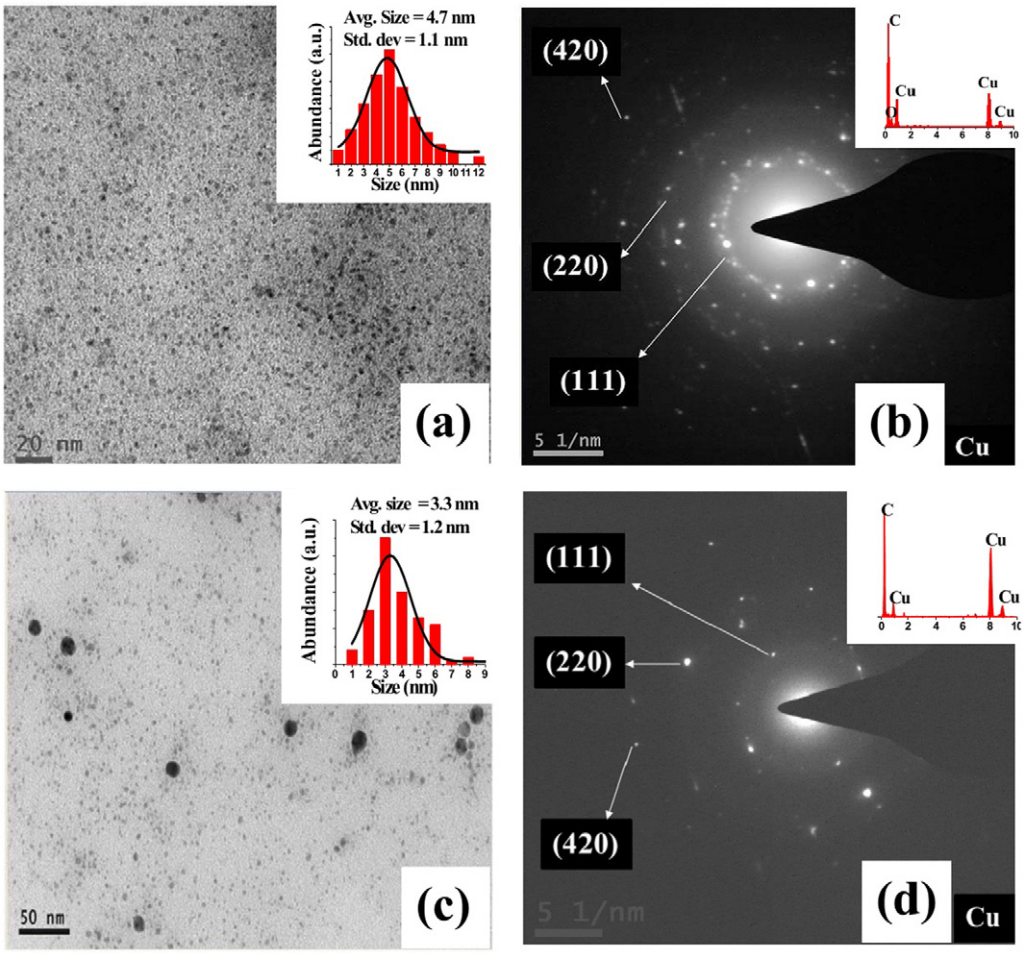

Figure 2. TEM imaging of (*a*) MCuNP1 (*c*) SCuNP1. Insets of (*a*) and (*c*) depict the NPs distribution (*b*) SAED spectra of the MCuNP1 and its corresponding EDAX data are shown in the inset (*d*) SAED spectra of the SCuNP1 and its corresponding EDAX data are shown in the inset.

3. Results and discussion

3.1. Characterizations of Cu colloids

Morphological studies and particle size measurements were performed by transmission electron microscopy (TEM), selected area electron diffraction pattern (SAED) and energy dispersive x-ray analysis (EDAX) with a FEI tecnai G2 S-Twin 200 kV instrument. TEM utilized carbon coated copper grids on which a tiny drop of metallic colloid was placed and dried for one day at room temperature. TEM images demonstrated the spherical morphology and well dispersion of NPs with different size distribution in acetone, DCM, ACN, and $CHCl_3$. TEM images of the MCuNP1, SCuNP1 are shown in figures 2(*a*) and (*c*) and their corresponding SAED patterns are illustrated in figures 2(*b*) and (*d*), respectively. Insets of figures 2(*a*) and (*c*) represent Cu NPs distribution with average sizes 4.7 ± 1.1 nm, 3.3 ± 1.2 nm, respectively, and insets of figures 2(*b*) and (*d*) depict the EDAX spectra. Polycrystalline nature of the Cu NPs in MCuNP1 and SCuNP1 resulted in concentric ring pattern in SAED (figures 2(*b*) and (*d*)). Estimated inter planar spacing (2.07 Å, 1.26 Å, 0.82 Å) was in good agreement with the interplanar spacing of pure copper miller planes (1 1 1), (2 2 0), and (4 2 0), respectively. This can be indexed with the standard pattern of the pure cubic phase of copper (PCPDF no 01-1242). Figure 2(*d*) illustrates SAED pattern with Miller indices (1 1 1), (2 2 0) and (4 2 0), and their corresponding interplanar spacings 2.09 Å, 1.27 Å and 0.8 Å, respectively. This was also indexed with the standard pattern of the pure cubic phase of copper (PCPDF no 04-0836). Likewise, figures 3(*a*) and (*c*) represent the TEM imaging of MCuNP2 and SCuNP2 in DCM and insets show NP distribution with average sizes 2.98 ± 0.85 nm, 3.7 ± 1.7 nm, respectively. Figures 3(*b*) and (*d*) depict the SAED pattern of MCuNP2 and SCuNP2, and the insets represent their respective EDAX spectra which emphasized the contribution of the Cu and chloride signatures in the NPs. The SAED pattern of both MCuNP2 and SCuNP2 revealed single crystalline nature. The measured inter planar spacings of 3.38 Å, 1.96 Å and 1.66 Å; 3.42 Å, 3.21 Å, 3.01 Å, 1.96 Å and 1.67 Å matched quite well with the lattice plane separations of CuCl (1 0 0), (1 1 0), and (1 1 2); CuCl (1 0 0), (0 0 2), (1 0 1), (1 1 0) and (1 1 2) (hexagonal phase, PCPDF no 09-0017), respectively. Figures 4(*a*) and (*c*) represent the TEM imaging of MCuNP3 and SCuNP3 in ACN with average sizes 29.2 ± 8.3 nm, 19 ± 6 nm, respectively. Figures 4(*b*) and (*d*) illustrate the SAED pattern of MCuNP3 and SCuNP3. MCuNP3 and SCuNP3 were polycrystalline in nature. Their interplanar spacings (2.50 Å, 2.27 Å, 1.70 Å, 1.29 Å and

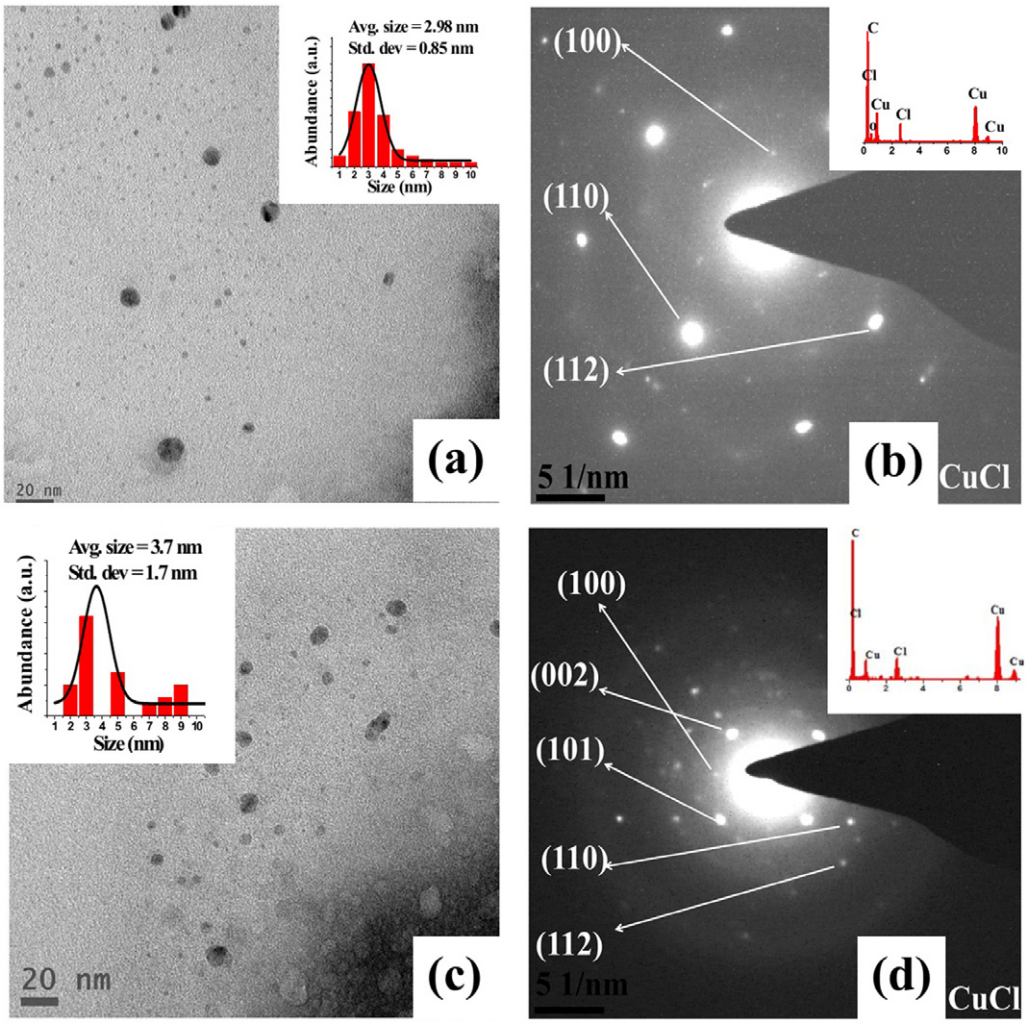

Figure 3. TEM imaging of (*a*) MCuNP2 (*c*) SCuNP2. Insets of (*a*) and (*c*) depict the NP distribution (*b*) SAED spectra of the MCuNP2 and its corresponding EDAX data are shown in the inset (*d*) SAED spectra of the SCuNP2 and its corresponding EDAX data are shown in the inset.

1.09 Å; 1.95 Å, 1.71 Å, 1.28 Å and 1.088 Å) from the SAED data were in agreement with the interplanar separations of CuO (Monoclinic phase, PCPDF no 65–2309) Miller planes ($\bar{1}$ 1 1), (2 0 0), (0 2 0), (2 2 1) and ($\bar{1}$ 3 1); CuO planes ($\bar{1}$ 1 2), (0 2 0), (2 2 1) and ($\bar{1}$ 3 1), respectively. Figures 5(*a*) and (*c*) represent the TEM images of MCuNP4 and SCuNP4 in chloroform with average sizes 13 ± 5 nm, 7.2 ± 1.7 nm, respectively. Figures 5(*b*) and (*d*) depict the SAED pattern of MCuNP4 and SCuNP4. Insets illustrate their respective EDAX spectra which emphasized the contribution from the Cu and chloride signatures in the NPs. Measured interplanar spacing of MCuNP4 (polycrystalline) and SCuNP4 (single crystalline) were 5.78 Å, 2.92 Å, 1.8 Å, 1.58 Å; 5.77 Å, 2.91 Å, 1.81 Å, which matched well with the plane separations (Monoclinic phase, PCPDF no 79–1635) of $CuCl_2$ (0 0 1), (2 0 0), (1 1 2) and (0 2 1); $CuCl_2$ (0 0 1), (0 0 2) and (1 1 2), respectively. Further investigations are needed and are underway to explain the single crystalline behaviour in SCuNP4. Miller planes corresponding to SAED ring patterns and their associated interplanar spacings (measured and reference values) are summarized in table 1. We believe that during the process of ablation, interaction between transient copper species with the chloride ions in the DCM resulted in the fabrication of CuCl NPs in MCuNP2 and SCuNP2. Similarly, $CuCl_2$ NPs were observed in MCuNP4 and SCuNP4 when ablation was carried out in chloroform. Since acetonitrile is highly capable of dissolving atmospheric oxygen, NPs in MCuNP3 and SCuNP3 were observed to be oxidized (CuO) to a greater extent than in acetone, DCM and chloroform. In the aspect of average sizes, single line ablation displayed better performance, whereas distribution and yield-wise multiple line ablation demonstrated better performance. Monitoring the quantity of matter on the TEM grid is not a reliable method to assert higher yield since the TEM is a local measurement. In fact, absorption spectra may be a more reliable technique to evaluate the yield in each case. The abundance of NPs was extrapolated from the bright field TEM images and found to be ∼1390 (900), ∼234 (75), ∼158 (71), and ∼690 (340) for MCuNP1 (SCuNP1), MCuNP2 (SCuNP2), MCuNP3 (SCuNP3), and MCuNP4 (SCuNP4), respectively. The conclusions obtained from the above characterizations were further strengthened by the analysis of UV-Vis absorption spectra.

UV-Vis absorption spectra (Jasco V-670) of colloids were recorded in the spectral range of 200–800 nm. Figure 6 depicts

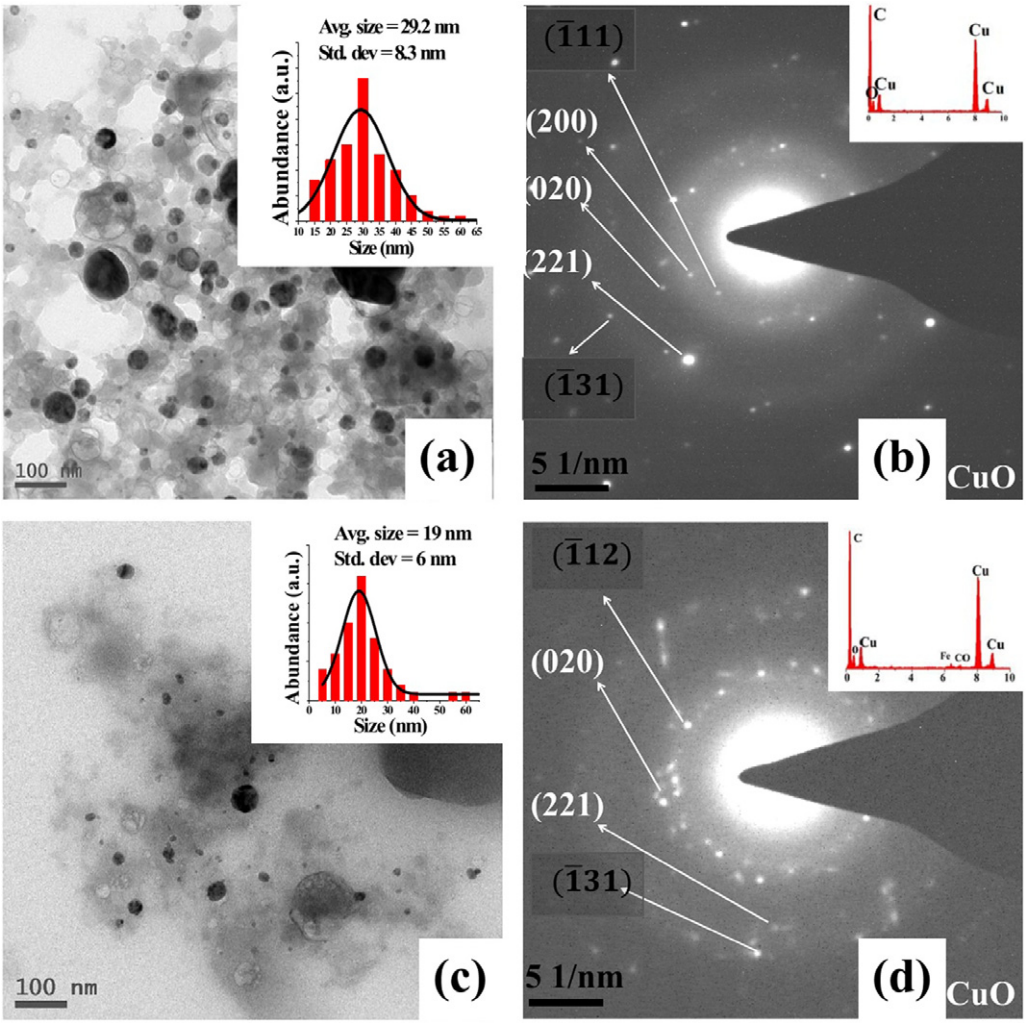

Figure 4. TEM imaging of (*a*) MCuNP3 (*c*) SCuNP3. Insets of (*a*) and (*c*) depict the NP distribution (*b*) SAED spectra of the MCuNP3 and its corresponding EDAX data are shown in the inset (*d*) SAED spectra of the SCuNP3 and its corresponding EDAX data are shown in the inset.

the whole absorption spectra of copper colloids prepared through both multiple and single line ablation while figure 7 illustrates only the spectral region within the vicinity of characteristic absorption peaks. Analysis of colloids for both schemes was accentuated with respect to the yield of NPs and their size distribution. MCuNP1 (figure 7(*a*)—red colour, solid curve), SCuNP1 (figure 7(*a*)—blue colour, dotted curve) colloids exhibited golden yellow colouration and SPR peak positions were observed near 580 nm and 566 nm, respectively. The peak position did not alter in both colloids even after several weeks which could be attributed to negligible aggregation effects since the electric dipole moment of acetone is high, resulting in possible formation of an electric double layer (EDL) [38] around the NPs. Surface chemistry may perhaps have played a significant role in preventing the aggregation. Characteristic absorption peak for MCuNP2 was observed near 371 nm (figure 7(*b*)—red colour, solid curve) while it was near 375 nm for SCuNP2 (figure 7(*b*)—blue colour, dotted curve). Probably, interim interaction of Cu ions in the plume with the Cl ions in the surrounding liquid medium resulted in formation of copper chloride NPs. Consequently, charge transfer between metal and the associated ligands [39] led to strong absorption of light in the UV spectral region. MCuNP3 (figure 7(*c*)—red colour, solid curve) exhibited light yellow–grey colouration with SPR peak near 601 nm and SCuNP3 (figure 7(*c*)—blue colour, dotted curve) near 588 nm, respectively, indicating that the plasmon peak was red-shifted (compared to Cu NPs in Acetone). In all likelihood, this could be due to increased thickness of oxide cladding surrounding the Cu NPs [40]. The interaction of NPs with air oxygen dissolved in ACN could have prevailed during the ablation, which led to a red shift of the SPR peak since the solubility of oxygen is high in ACN at room temperature [41]. The absorbance in the case of NPs in ACN was an order of magnitude lower compared to others. This could, possibly, be due to two main reasons: (1) if particle sizes are large, higher order polarization resulting from quadrupole, octopole oscillations usually dominate. In general, these multi-pole oscillations have less probability of absorption compared to dipole oscillations; (2) if the oxide cladding on the metallic NP is thick then it diminishes the influence of the incident field. Similarly, MCuNP4 (figure 7(*d*)—red colour, solid curve), SCuNP4 (figure 7(*d*)—blue colour, dotted curve), exhibited characteristic absorption peaks near 383 nm, 375 nm,

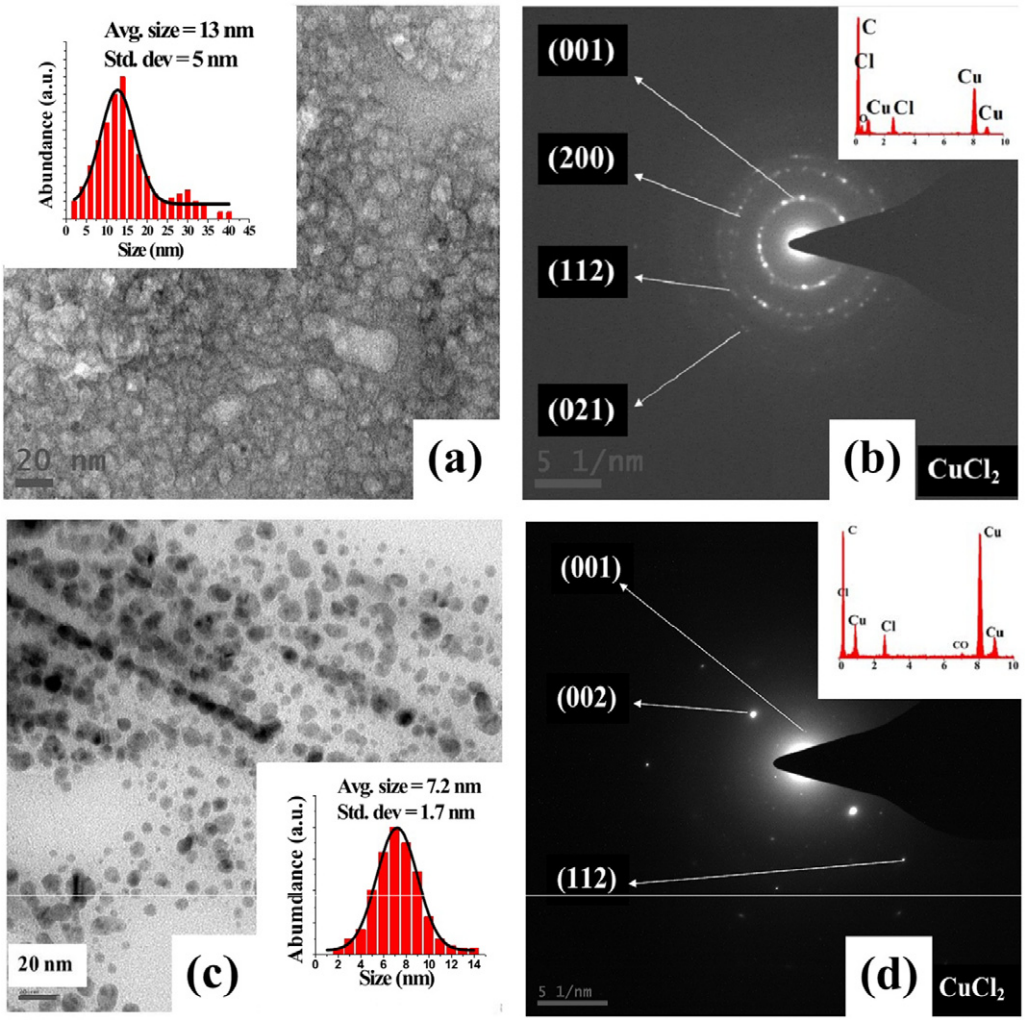

Figure 5. TEM imaging of (*a*) MCuNP4 (*c*) SCuNP4. Insets of (*a*) and (*c*) depict the NP distribution (*b*) SAED spectra of the MCuNP4 and its corresponding EDAX data are shown in the inset (*d*) SAED spectra of the SCuNP4 and its corresponding EDAX data are shown in the inset.

respectively. Among the two cases, multiple line ablation was observed to provide higher absorbance compared to single line ablation. This observation revealed that the yield of the NPs was higher in multiple line ablation than in the case of single line ablation. It was apparent from the UV-Vis absorption spectra that characteristic peak position of the colloids obtained through multiple line ablation was red-shifted compared to colloids obtained using single line ablation. Only in the case of DCM were the sizes of NPs in MCuNP2 smaller than those obtained in SCuNP2, because of which we observed a small blue shift rather than a red shift. The reason for the discrepancy is not yet clearly understood. We believe that the solvent properties played a major role and further investigations are pending in this direction to understand the complete mechanism.

In an earlier study Miranda *et al* [42, 43] performed the fabrication of Cu NPs in liquid media with nanosecond laser pulses. The writing conditions [44] in their experiments were different from the present experiments. In our case laser beam was scanned on the surface of the Cu substrate to draw periodic lines with a given separation rather than mere focusing. In general, below ablation threshold polished surface will not melt [45], whereas a roughened surface (ablated multiple times) would offer loosely bound micro-protrusions to the laser beam which decreases the ablation threshold. In the case of multiple line ablation, inhomogeneity could have resulted in a non-uniform melting of tips and micro-protrusions thereby reducing the ablation threshold and consequently increased yield. Higher yield of Cu NPs in multiple line ablation case was confirmed from the observed large plasmon bandwidth of colloids as explained by Garcia [46]. Since NPs in MCuNP1, MCuNP2, MCuNP3 and MCuNP4 had higher density compared to corresponding SCuNP1, SCuNP2, SCuNP3 and SCuNP4 the net electric field at the NP site is summation of the field due to incident light and the field created by the remaining NPs. Accordingly, resonance condition gets modified resulting in a red shift of the characteristic absorption band [46].

3.2. Raman characterization of colloids

The organic solvents in which ablation was carried out were collected in air tightened glass bottles and the Raman spectra were recorded from these colloids prepared through

Table 1. Summary of the SAED data including references for MCuNP1–MCuNP4 and SCuNP1–SCuNP4.

SAED planes and inter planar spacing value in Å												
MCuNP1		SCuNP1		MCuNP2	SCuNP2		MCuNP3	SCuNP3		MCuNP4	SCuNP4	
PCPDF no. 01-1242		PCPDF no. 04-0836		PCPDF no. 09-0017			PCPDF no. 65–2309			PCPDF no. 79–1635		
Expt	Ref.	Expt	Ref.	Expt		Ref	Expt		Ref.	Expt.		Ref.
(1 1 1) 2.07 Å	(1 1 1) 2.08 Å	(1 1 1) 2.09 Å	(1 1 1) 2.088 Å	(1 0 0) 3.38 Å	(1 0 0) 3.42 Å	(1 0 0) 3.395 Å	($\bar{1}$ 1 1) 2.50 Å		($\bar{1}$ 1 1) 2.515 Å	(0 0 1) 5.78 Å	(0 0 1) 5.77 Å	(0 0 1) 5.774 Å
(2 2 0) 1.26 Å	(2 2 0) 1.27 Å	(2 2 0) 1.27 Å	(2 2 0) 1.278 Å		(0 0 2) 3.21 Å	(0 0 2) 3.208 Å	(2 0 0) 2.27 Å		(2 0 0) 2.299 Å	(2 0 0) 2.92 Å	(2 0 0) 2.91 Å	(2 0 0) 2.921 Å
(4 2 0) 0.82 Å	(4 2 0) 0.81 Å	(4 2 0) 0.80 Å	(4 2 0) 0.808 Å		(1 0 1) 3.01 Å	(1 0 1) 2.997 Å		($\bar{1}$ 1 2) 1.95 Å	($\bar{1}$ 1 2) 1.955 Å	(1 1 2) 1.8 Å	(1 1 2) 1.81 Å	(1 1 2) 1.812 Å
				(1 1 0) 1.96 Å	(1 1 0) 1.96 Å	(1 1 0) 1.953 Å	(0 2 0) 1.70 Å	(0 2 0) 1.71 Å	(0 2 0) 1.708 Å	(0 2 1) 1.58 Å		(0 2 1) 1.586 Å
				(1 1 2) 1.66 Å	(1 1 2) 1.67 Å	(1 1 2) 1.668 Å	(2 2 1) 1.29 Å	(2 2 1) 1.28 Å	(2 2 1) 1.291 Å			
							($\bar{1}$ 3 1) 1.09 Å	($\bar{1}$ 3 1) 1.088 Å	($\bar{1}$ 3 1) 1.088 Å			

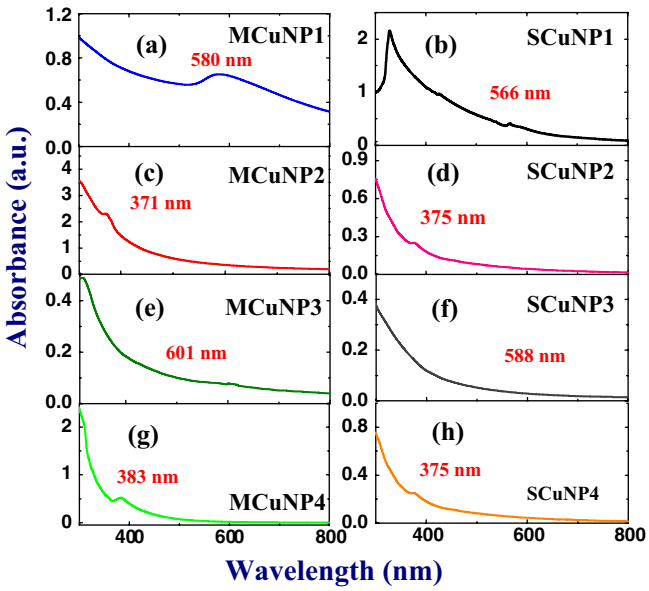

Figure 6. UV-Vis absorption spectra of Cu NPs prepared through ps laser ablation in (*a*) acetone, multiple line ablation (MCuNP1) (*b*) acetone, single line ablation (SCuNP1) (*c*) DCM, multiple line ablation (MCuNP2) (*d*) DCM, single line ablation (SCuNP2) (*e*) acetonitrile, multiple line ablation (MCuNP3) (*f*) acetonitrile, single line ablation SCuNP3 (*g*) chloroform, multiple line ablation (MCuNP4) (*h*) chloroform, single line ablation (SCuNP4).

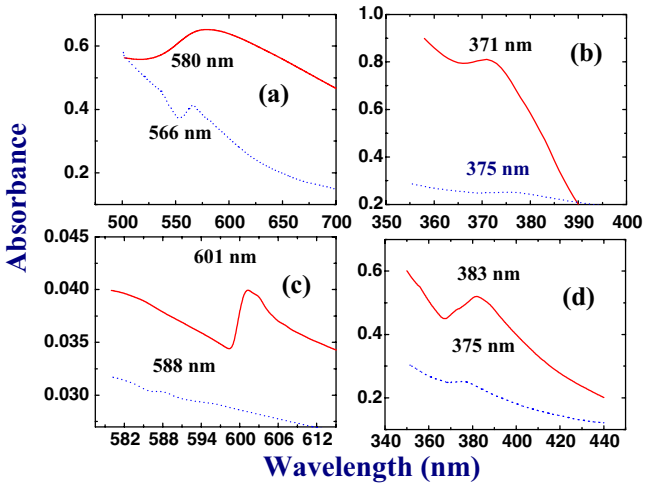

Figure 7. Expanded UV-Vis absorption spectra of Cu NPs prepared through ps laser ablation in (*a*) acetone (MCuNP1, SCuNP1), (*b*) DCM (MCuNP2, SCuNP2), (*c*) acetonitrile (MCuNP3, SCuNP3) and (*d*) chloroform (MCuNP4, SCuNP4). Solid lines represent MCuNPs while dotted lines represent SCuNPs.

multiple/single line ablation techniques. Raman spectra from the colloids were recorded using 785 nm solid state laser (∼0.5 mW) and a spectrometer (Ocean optics) coupled to a fibre. The colloidal Cu NPs were taken in 1 cm cuvette, placed along the beam propagation direction and the Raman spectra were recorded directly from solutions. The acquisition time for each measurement was 5 s. All the spectra were calibrated with respect to the signature at 520 cm^{-1} of silicon wafer. Figure 8 illustrates the Raman spectra recorded for (*a*) MCuNP1 and SCuNP1 (*b*) MCuNP2 and SCuNP2 (*c*) MCuNP3 and SCuNP3 (*d*) MCuNP4 and SCuNP4, respectively. In the case of MCuNP1 (figure 8(*a*)—blue, top curve) the Raman signal intensity for the 531.04 cm^{-1} mode was ∼2179 (with background correction), whereas the Raman intensity for pure Acetone (figure 8(*a*)—red, bottom curve) was ∼9. The intensity enhancement was estimated to be ∼242. Some of the peaks merged in the background in normal Raman spectra of acetone were detected in the spectra of MCuNP1. Raman spectra of SCuNP1 are illustrated in figure 8(*a*)—wine, middle curve. The primary observation was that elevation of the Raman signatures in MCuNP1 was predominant as compared to SCuNP1. In the case of MCuNP2, SCuNP2 (figure 8(*b*)—blue, top curve; figure 8(*b*)—red, bottom curve) the intensity enhancements compared to the Raman signatures of pure DCM were ∼11, 5 for 283.4 cm^{-1} mode, ∼5.5, 5 for the 701.6 cm^{-1} mode, respectively. In addition to the observed modes MCuNP2 elevated the 739.3 cm^{-1} (which was not observed in SCuNP2) with an intensity enhancement of ∼72. In the case of MCuNP3, SCuNP3 (figure 8(*c*)—blue, top curve;

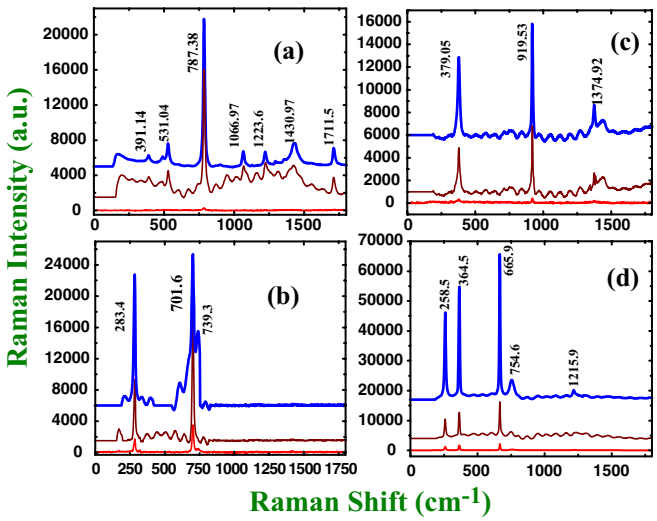

Figure 8. Raman spectra of (*a*) MCuNP1 (blue/top), SCuNP1 (wine/middle) and pure acetone (red/bottom), (*b*) MCuNP2 (blue/top), SCuNP2 (wine/middle) and pure DCM (red/bottom), (*c*) MCuNP3 (blue/top), SCuNP3 (wine/middle) and pure ACN (red/bottom), (*d*) MCuNP4 (blue/top), SCuNP4 (wine/middle) and pure chloroform (red/bottom) recorded with an excitation wavelength of 785 nm and an integration time of 5 s.

figure 8(*c*)—red, bottom curve) the intensity enhancements compared to the Raman signatures of pure ACN were ∼54.8, 30.7 for the 379.05 cm^{-1} mode, ∼50, 29.6 for the 919.53 cm^{-1} mode, and ∼16.3, 11.6 for 1374.92 cm^{-1} mode, respectively. Similarly, in the case of MCuNP4, SCuNP4 (figure 8(*d*)—blue, top curve; figure 8(*d*)—red, bottom curve) the intensity enhancements compared to the Raman signatures of pure $CHCl_3$ were ∼26.9, 5.6 for the 258.5 cm^{-1} mode, ∼24.5, 5.1 for the 364.5 cm^{-1} mode, ∼24.5, 5.8 for 665.9 cm^{-1} mode and 51.3, 10.9 for 754.6 cm^{-1}, respectively. In addition to the mentioned modes, MCuNP4 elevated the 1215.9 cm^{-1} (which was again not observed in SCuNP4) with an intensity enhancement of ∼92. Observed modes of the Cu colloids are consistent with reported Raman modes of acetone [47], DCM [48], ACN [49] and chloroform [50]. All other Raman active modes of the solvents and corresponding intensity enhancements are summarized in table 2. Raman spectra obtained from multiply and singly ablated Cu colloids were compared with the Raman spectra of the pure solvents to estimate the intensity enhancement. During the ablation process Cu NPs were fabricated with some residual surface charge and the interaction of polar molecules with the charged surfaces resulted in direct adsorption of molecules on NPs surfaces. Consequently, irradiation of colloids with laser results in local field intensity enhancements leading to an amplification of the Raman signals which could be considered as SERS. As per the Raman spectra obtained from Cu NPs prepared through multiple/single line ablation, it was evident that colloids prepared via multiple line ablation demonstrated better enhancement in the Raman signatures of the solvent molecules than those prepared through single line ablation. In the present studies we could not identify the signatures of by-products through recorded Raman spectra since enhancement of the Raman modes of solvent molecules (stimulated by the presence of Cu NPs) could have suppressed the signatures of by-products.

3.3. NLO studies

The third order NLO properties of the NPs were investigated at a wavelength of 800 nm with ∼2 ps pulses using the standard *Z*-scan technique [51, 52]. Complete features of the experimental setup are reported in some of our earlier works [53–57]. Open aperture *Z*-scan data provides information about the nonlinear absorption (related to imaginary part of third order NLO susceptibility, $\chi^{(3)}$) properties while the closed aperture (CA) *Z*-scan data provides information on sign and magnitude of the nonlinear refractive index n_2 (related to the real part of $\chi^{(3)}$). The linear transmittance was typically >95% for all the NPs except for MCuNP1 and MCuNP3 (>80%). Figure 9 depicts the complete open aperture data obtained for all investigated eight NPs at both lower (open squares—80 GW cm^{-2}) and higher (open stars—125 GW cm^{-2}) peak intensities. Three distinct behaviours were observed: (a) reverse saturable absorption (RSA) type of behaviour which could be attributed to two-photon absorption (2PA; β), (b) an effective three-photon absorption (3PA; γ_{eff}) type of behaviour and (c) a switching mechanism from saturable absorption (SA) to RSA. The open aperture data of MCuNP1 (figure 9(*a*)) and MCuNP3 (figure 9(*e*)) illustrates the behaviour of switching from SA to RSA at lower peak (open squares—80 GW cm^{-2}) intensity and pure RSA at higher peak intensity (open stars—125 GW cm^{-2}). The data obtained at higher peak intensities was fitted efficiently using only β. At lower peak intensity, SCuNP1 (figure 9(*b*)) data was fitted to β while SCuNP3 (figure 9(*f*)) did not show any NLO behaviour. At higher peak intensity, both the samples SCuNP1 and SCuNP3 exhibited RSA type of behaviour and the data was fitted successfully using γ_{eff} [2PA + ESA] and β, respectively. The resonances of SCuNP1 (565 nm and 310 nm) and SCuNP3 (588 nm) might have led to this observation. The open aperture data of MCuNP2 (figure 9(*c*)), SCuNP2 (figure 9(*d*)), MCuNP4 (figure 9(*g*)) and SCuNP4 (figure 9(*h*)) revealed that 2PA was dominant at both peak intensities with 800 nm excitation which can be accredited to the characteristic absorption band of nano colloids formed at nearly 400 nm.

It is extremely difficult to model the nonlinear absorption independently for NPs of different sizes and composition [58]. In such materials [59–60] the contributions to nonlinear absorption can result from electrons participating in the following transitions: (a) completely occupied 'd' band to unoccupied conduction band and/or (b) within the conduction band (ground states to excited states) due to plasmon resonances [61] and (c) free carrier absorption from excited conduction band to high lying states. Figure 10 depicts a generic energy band diagram portraying various mechanisms of (a) saturable absorption: in the case of MCuNP1 and McuNP3 we observed residual absorption at 800 nm and, therefore, expect saturation at lower peak intensities with probable transition from 'd' band to the 'p' (conduction) band depicted by Ia in figure 10. However, at higher peak intensities one expects 2PA as depicted by Ib with

Table 2. Observed active Raman modes and their corresponding Raman intensity enhancements of the organic solvents of Cu colloids with an excitation wavelength 785 nm. Raman intensity enhancements of the colloidal solvents were estimated with respect to the Raman signals of the pure solvents. Time of integration was 5 s. Rep.: reported, Obs.: observed.

Acetone				DCM				ACN				Chloroform			
Raman active mode (cm^{-1})		Raman intensity enhancement		Raman active modes (cm^{-1})		Raman intensity enhancement		Raman active modes (cm^{-1})		Raman intensity enhancement		Raman active mode (cm^{-1})		Raman intensity enhancement	
Rep.	Obs.	MCuNP1	SCuNP1	Rep.	Obs.	MCuNP2	SCuNP2	Rep.	Obs.	MCuNP3	SCuNP3	Rep.	Obs.	MCuNP4	SCuNP4
391.5	391.14	46	35	285	283.4	11	5	377.4	379.05	54.8	30.7	262	258.5	26.9	5.6
530	531.04	242.4	175.8	703	701.6	5.5	5	917.7	919.53	49.6	29.6	365	364.5	24.5	5.1
788	787.38	96.14	77.3	738	739.3	71.9	Not observed	1373.9	1374.9	16.3	11.6	668	665.9	24.5	5.8
1067.4	1066.9	80	74									750	754.6	51.3	11
1223.8	1223.6	78	78.5									1216	1215.9	91.2	Not observed
1430.5	1430.9	94.6	60.4												
1711	1711.5	29.3	26.8												

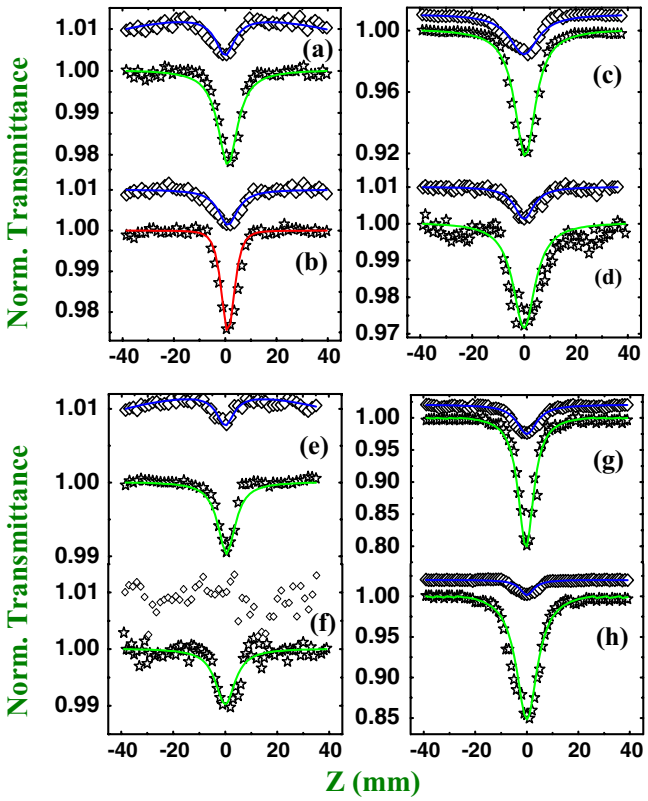

Figure 9. Open aperture Z-scan curves obtained for (a) MCuNP1 (b) SCuNP1 with varying input intensities $I_{00} = 80\,\mathrm{GW\,cm^{-2}}$ (open squares), $I_{00} = 125\,\mathrm{GW\,cm^{-2}}$ (open stars). Open aperture Z-scan curves obtained for (c) MCuNP2 (d) SCuNP2 with varying input intensities $I_{00} = 80\,\mathrm{GW\,cm^{-2}}$ (open squares), $I_{00} = 125\,\mathrm{GW\,cm^{-2}}$ (open stars). Open aperture Z-scan curves obtained for (e) MCuNP3 (f) SCuNP3 with varying input intensities $I_{00} = 80\,\mathrm{GW\,cm^{-2}}$ (open squares), $I_{00} = 125\,\mathrm{GW\,cm^{-2}}$ (open stars) and (g) MCuNP4 (h) SCuNP4 with varying input intensities $I_{00} = 80\,\mathrm{GW\,cm^{-2}}$ (open squares), $I_{00} = 125\,\mathrm{GW\,cm^{-2}}$ (open stars). Solid lines are the theoretical fits.

transitions from ground state conduction band (GSCB) to excited state conduction band (ESCB). Due to two-photon resonance (800 nm + 800 nm) between GSCB and ESCB, 2PA dominates with negligible contribution from SA at higher peak intensities, (b) instantaneous 2PA with possible mechanisms are depicted in the second box marked as IIa (between 'd' band and GSCB) and IIb (between GSCB and ESCB), (c) two-step 3PA (2PA + ESA) at very high peak intensities as depicted by processes in box IIIa and IIIb (excited state absorption induced from ESCB in this case). The figure is generic in the sense that we have assumed a fixed gap between the states and different photon energies, whereas in reality the band gaps could be different (including SPR positions) for these eight different NPs with single energy photon excitation (1.55 eV for 800 nm ps photon).

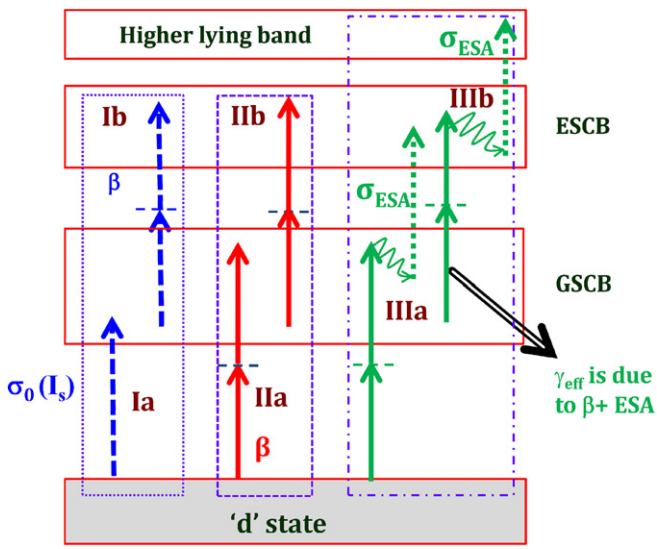

Figure 10. A generalized energy band diagram of the observed CuNPs (pure Cu NPs, CuO NPs, CuCl NPs, $CuCl_2$ NPs) explaining various nonlinear absorption phenomena. ESCB refers to excited state conduction band, GSCB refers to ground state conduction band.

We had earlier modelled such complicated nonlinear absorption phenomena in different organic moieties and the relevant equations are documented in our earlier publications [53–57, 62, 63]. A similar approach was used and the experimental data was fitted with appropriate equations to estimate nonlinear absorption coefficients. Amongst all,

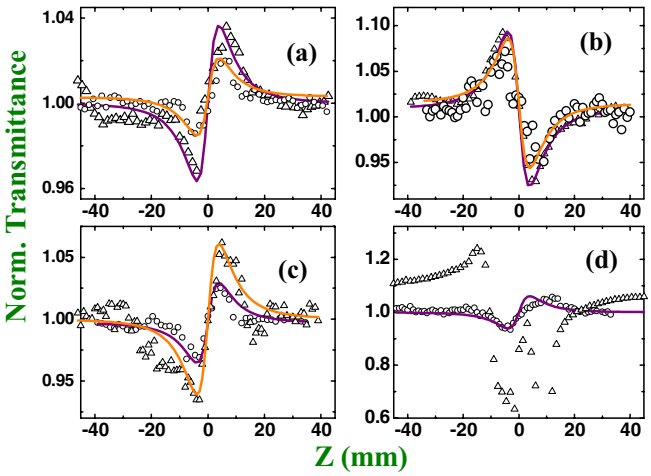

Figure 11. CA Z-scan curves obtained for (a) MCuNP1 (open triangles), SCuNP1 (open circles) (b) MCuNP2 (open triangles), SCuNP2 (Open circles) (c) MCuNP3 (open triangles), SCuNP3 (open circles) (d) MCuNP4 (open triangles), SCuNP4 (open circles). CA studies were performed at a peak intensity of 33 GW cm^{-2}. Solid lines are the theoretical fits.

MCuNP4 exhibited largest β, n_2, and $\chi^{(3)}$ values. The values of nonlinear refractive index (n_2) were obtained for all colloidal solutions at an intensity of 33 GW cm^{-2} using CA Z-scan method and the data is shown in figure 11. Figure 11(a) illustrates the CA data of MCuNP1 (triangles) and SCuNP1 (circles) which exhibit positive nonlinearities (like solvent) with $n_2 = 9 \times 10^{-16}$ cm^2/W and $n_2 = 4 \times 10^{-16}$ cm^2/W, respectively, smaller than the solvent magnitude ($n_2 = 19 \times 10^{-16}$ cm^2/W) and the observed sign of n_2 for MCuNP1 and SCuNP1 was negative. Figures 11(b)–(d) represent CA data of MCuNP2 (SCuNP2), MCuNP3 (MCuNP3) and MCuNP4 (MCuNP4). The observed sign of the nonlinearity is negative (negative) for MCuNP2 (SCuNP2), positive (positive) for MCuNP3 (MCuNP3) and negative (positive). The data was fitted using standard equations [64] to estimate the magnitudes of n_2. The contribution from solvents (DCM, ACN and chloroform) (positive nonlinearity) was also identified. The estimated nonlinear coefficients corresponding to all the NPs are listed in table 3. There have been few reports [65–67] of NP fragmentation using short laser pulses. In an earlier report [68] simultaneous occurrence of fragmentation and optical nonlinearity were observed with metal NPs. In the process of scanning a sample across the focus there could have been fragmentation occurring in the NPs studied in our case. The Z-scans were performed 2–3 times and the values of coefficients observed were within the experimental error range (±15%). The values cited are an average value of these measurements. We had also recorded the UV-Vis absorption spectra of the colloidal solutions before and after the Z-scans and we could not record any major differences in the plasmon peak position/width, again within the experimental errors of our measurements. The fluences corresponding to our Z-scan measurements and were found to be ~0.52 J cm^{-2} (for minimum input energy of 2 μJ and assuming a spot size radius of 35 μm; $F = E_{in}/\pi \times \omega^2$) and ~1.04 J cm^{-2} (for maximum input energy of 4 μJ and assuming a spot size of 35 μm). The amount of time NPs were exposed to such fluences was ~10 s. The fragmentation, if it occurred at all, would be within the focal volume of the beam which was few μl, whereas the cuvette (1 mm path length) can hold 0.35 ml, which probably could be the reason for absorption spectra not revealing any spectral changes. Furthermore, the NLO coefficients measured were within an experimental error of ±15%. Further detailed studies will be necessary to completely evaluate the fragmentation effects on the NLO coefficients. The magnitudes obtained in our case are compared with coefficients of some of the recently synthesized and reported NPs [69–80] and the data is shown in table 4. Some of the reported coefficients were stronger in magnitude than those of ours since, (a) they used longer pulses (ns) for measurements compared to short pulses (2 ps) in our case, (b) in their case excitation was close to SPR and, therefore, is expected to enhance the nonlinearities. In our case the coefficients obtained (except for MCuNP1 and MCuNP3) are in the non-resonant domain. Comparison of the obtained NLO coefficients revealed the magnitudes of nonlinearities were generally higher for multiply ablated NPs compared to singly ablated NPs. The outcome of the Raman investigations could be explained as probably due to the consequence of combined surface plasmon resonances (hot spots) from the agglomerated individual Cu NPs in certain cases. It was established that multiple line ablation led to the higher yield compared to the single line ablation and consequently the degree of agglomeration [81, 82] in colloids prepared through multiple line ablation was greater than in the single line ablation colloids. Because of this, colloids prepared through multiple line ablation might support the formation of a higher number of hot spots than the colloids prepared through single line ablation. However, further investigations are required to ascertain these issues.

4. Conclusions

In summary, an extensive study pertaining to fabrication of Cu NPs via ps laser multiple/single line ablation were carried out in organic liquids and their spectroscopic, Raman characterization, and NLO studies were carried out. Combined effect of scan separation and the beam diameter ($2\omega_0$) at the focus resulted in different writing conditions namely multiple (line separation (5 μm) < spot diameter (50 μm)) and single (line separation (60 μm) > spot diameter (50 μm)) ablation which led to differences in the yield and average size of the NPs. Additionally, the interaction of transient metallic plume with the constituents of surrounding liquid and its dependence on the intrinsic nature of the liquid media led to the fabrication of pure Cu (MCuNP1/SCuNP1), CuCl (MCuNP2/SCuNP2), CuO (MCuNP3/SCuNP3) and $CuCl_2$ (MCuNP4/SCuNP4) NPs and the obtained results are discussed in detail. Investigation of optical nonlinearities revealed that colloids prepared through the multiple line ablation exhibited strong nonlinearities compared to the counterparts of single line ablation since the yield was higher in the multiple line ablation than in single line ablation. This could be probably due to the agglomeration effects which resulted in the formation of hot spots. Similarly,

Table 3. Measured NLO coefficients of Cu colloids prepared through multiple and single line ablation techniques in acetone, DCM, ACN, and Chloroform at different peak intensities.

Peak intensity ($GW\,cm^{-2}$)	Sample	β ($cm\,W^{-1}$) $\times 10^{-11}$ and (I_S ($W\,cm^{-2}$) $\times 10^7$)	n_2^a ($cm^2\,W^{-1}$) $\times 10^{-15}$	$\lvert\chi^{(3)}\rvert_{(e.s.u)}$ $\times 10^{-13}$	Size (nm)
82	MCuNP1	0.10 [2.90]	0.90	0.80	4.7 ± 1.1
	SCuNP1	0.40	0.40	0.35	3.3 ± 1.2
125	MCuNP1	0.52	—	—	—
	SCuNP1	$\gamma_{eff} = 1.70 \times 10^{-22}\,cm^3\,W^{-2}$	—	—	—
82	MCuNP2	0.90	—	—	—
	SCuNP2	0.30	—	—	—
125	MCuNP2	1.40	−2.00	1.78	2.98 ± 0.85
	SCuNP2	0.70	−1.30	1.15	3.7 ± 1.7
82	MCuNP3	0.05 [2.00]	—	—	—
	SCuNP3	—	—	—	—
125	MCuNP3	0.23	1.20	1.07	29.2 ± 8.3
	SCuNP3	0.33	0.80	0.71	19 ± 6
82	MCuNP4	1.50	—	—	—
	SCuNP4	0.67	—	—	—
125	MCuNP4	6.00	−2.10	1.90	13 ± 5
	SCuNP4	1.20	1.40	1.21	7.2 ± 1.7

[a] n_2 was calculated using 33 $GW\,cm^{-2}$.

Table 4. Summary of NLO coefficients of copper NPs synthesized using different techniques.

Sample	Preparation method	Laser wavelength and pulse width	β or α_2 ($cm\,W^{-1}$)	n_2 ($cm^2\,W^{-1}$)	[$\chi^{(3)}$] (e.s.u.)	Ref.
Cu nanocomp.	Ion implantation	532 nm and 7 ns 26 ps (10 Hz)			8.8×10^{-10} 8.4×10^{-11}	[69]
PGO film with Cu/Cu_2O NPs	Melting process	800 nm and 150 fs (76 MHz)			6.8×10^{-10}	[70]
$Cu:SiO_2$ nanoparticle composite	Ion implantation	540–610 nm and 200 fs			$(1.6–3.1)\times10^{-9}$	[71]
Cu/SiO_2 composition	Ion implantation	532 nm 1064 nm and 38 ps (10 Hz)			2.1×10^{-7} 1.2×10^{-7}	[72]
Cu/SiO_2films	Multi target sputtering method	590 nm and 150 fs			1.8×10^{-10}	[73]
CuNPs in ZnO matrix	Ion implantation (high dose)	532 nm, 7.5 ns 55 ps	5.46×10^{-3} 2.07×10^{-3}			[74]
SG : Cu and SLSG : Cu	Ion implantation	1064 nm and 35 ps			37.8 and 9.56×10^{-10}	[75]
$Cu:Bi_2O_3$ nanocomposites film	Multi target magnetron sputtering	800 nm and 120 fs (10 Hz)	0.11×10^{-6}	-0.78×10^{-11}	1.45×10^{-9}	[76]
$Cu:Al_2O_3$	Pulsed laser deposition	596 nm and 6 ps (3.8 MHz)	$(0.75–0.5)\times10^{-4}$	$-(0.25–0.38)\times10^{-9}$		[77]
$Cu:Al_2O_3$	Pulsed laser deposition	596 nm and 6 ps (3.8 MHz)	-2.34×10^{-5}	2.93×10^{-10}		[78]
$Cu:Al_2O_3$	Pulsed laser deposition	600 nm and 7 ps	$(0.8–4) \times 10^{-5}$	$(0.9–10) \times 10^{-10}$		[79]
Cu colloidal solutions	Chemical synthesis	532 nm 1064 nm, 35 ps			$(19 \pm 9.5) \times10^{-15}$ $(5.8 \pm 2.9) \times10^{-15}$	[80]

recorded Raman spectra from the organic liquids in which ablation took place revealed good enhancement of the Raman signatures (from the estimated Raman intensity enhancements) in multiple line ablation case compared to single line ablation case. Maximum intensity enhancement was observed for the Cu colloids in acetone ∼243 (∼175) prepared through multiple (single) line ablation techniques. Finally, we conclude that multiple line ablation demonstrated advantages over single line ablation for generating NPs for applications in the fields of SERS and photonics. Our future studies include (a) detailed morphological investigation of nanostructures (NSs) on the target left after ablation for applications in SERS, (b) feasibility studies for combining NPs and NSs for further enhancement in SERS signals and (c) exploration of the anti-bacterial properties of Cu NPs generated in different liquids.

Acknowledgments

We are grateful to DRDO for financial support. We acknowledge the support of Mr Sreedhar during some of the experiments carried out with ps pulses. A fruitful discussion with Dr P Prem Kiran is also acknowledged.

References

[1] Binh N T, Khanh T T V, Quang D N, Dinh N T, Nguyen A T and Hue T T 2012 Preparation of metal nanoparticles for surface enhanced Raman scattering by laser ablation method *Adv. Nat. Sci.: Nanosci. Nanotechnol.* **3** 025016

[2] Li Z, Hattori H T, Parkinson P, Tian J, Fu L, Tan H H and Jagadish C 2012 A plasmonic staircase nano-antenna device with strong electric field enhancement for surface enhanced Raman scattering (SERS) applications *J. Phys. D: Appl. Phys.* **45** 305102

[3] Sakano T, Tanaka Y, Nishimura R, Nedyalkov N N, Atanasov P A, Saiki T and Obara M 2008 Surface enhanced Raman scattering properties using Au-coated ZnO nanorods grown by two-step, off-axis pulsed laser deposition *J. Phys. D: Appl. Phys.* **41** 235304

[4] Sekhar H and Narayana Rao D 2012 Preparation, characterization and nonlinear absorption studies of cuprous oxide nanoclusters, micro-cubes and micro-particles *J. Nanopart. Res.* **14** 976–86

[5] Faraji N, Younus W M M, Kharazmi A, Saion E, Shahmiri M and Tamchek N 2012 Synthesis, characterization and nonlinear optical properties of silver/PVA nanocomposites *J. Eur. Opt. Soc. Rapid Publ.* **7** 12040

[6] Dou X, Chung PY, Jiang P and Dai J 2012 Surface plasmon resonance-enabled antibacterial digital versatile discs *Appl. Phys. Lett.* **100** 063702

[7] Singh S C and Zeng H 2012 Nanomaterials and nanopatterns based on laser processing: a brief review on current state of art *Sci. Adv. Mater.* **4** 368–90

[8] Wagener P, Ibrahimkutty S, Andreas M, Anton P and Barcikowski S 2013 Dynamics of silver nanoparticles formation and agglomeration inside the cavitation bubble after pulsed laser ablation in liquid *Phys. Chem. Chem. Phys.* **15** 3068–74

[9] Tilaki R M, Iraji zad A and Madhavi S M 2007 Size, composition and optical properties of copper nanoparticles prepared by laser ablation in liquids *Appl. Phys.* A **88** 415–9

[10] Yang G W 2007 Laser ablation in liquids: applications in the synthesis of nanocrystals *Prog. Mater. Sci.* **52** 648–98

[11] Fumitaka M, Kohno J, Takeda Y and Kondow T 2001 Formation of gold nanoparticles by laser ablation in aqueous solution of surfactant *J. Phys. Chem.* B **105** 5114–20

[12] Bozon-Verduraz F, Brayner R, Voronov V V, Kirichenko N A, Simakin A V and Shafeev G A 2003 Production of nanoparticles by laser-induced ablation of metals in liquids *Quantum Electron.* **33** 714–20

[13] Tarasenko N V, Butsen A V and Nevar E A 2005 Laser-induced modification of metal nanoparticles formed by laser ablation technique in liquids *Appl. Surf. Sci.* **247** 418–22

[14] Bozon-Verduraz F, Brayner R, Voronov V V, Kirichenko N A, Simakin A V and Shafeev G A 2003 Production of nanoparticles by laser-induced ablation of metals in liquids *Quantum. Electron.* **33** 714–20

[15] Aye H L, Choopun S and Chairuangsri T 2010 Preparation of nanoparticles by laser ablation on copper target in distilled water *Adv. Mater. Res.* **93–94** 83–6

[16] Leonard K, Kurawaki J, Hayakawa K, Thein Tun M and Kusumoto Y 2009 Preparation and characterization of copper(II) tetrasulfonated phthalocyanine nanoparticles formed by laser ablation in poor solvents *Colloid Polym. Sci.* **287** 773–8

[17] Saito M, Yasukawa K, Umeda T and Aoi Y 2008 Copper nanoparticles fabricated by laser ablation in polysiloxane *Opt. Mater.* **30** 1201–4

[18] Malyavantham G, O'Brien D T, Becker M F, Keto J W and Kovar D 2004 Au–Cu nanoparticles produced by laser ablation of mixtures of Au and Cu microparticles *J. Nanopart. Res.* **6** 661–4

[19] Kazakevich P V, Voronov V V, Simakin A V and Shafeev G A 2004 Formation of copper and brass nanoparticles upon laser ablation in liquids *Quantum Electron.* **34** 951–6

[20] Burakov V S, Tarasenko N V, Butsen A V, Rozantsev V A and Nedel'ko N I 2005 Formation of nanoparticles during double-pulse laser ablation of metals in liquids *Eur. Phys. J. Appl. Phys.* **30** 107–12

[21] Amendola V, Polizzi S and Meneghetti M 2007 Free silver nanoparticles synthesized by laser ablation in organic solvents and their easy functionalization *Langmuir* **23** 6766–70

[22] Amendola V and Meneghetti M 2009 Laser ablation synthesis in solution and size manipulation of noble metal nanoparticles *Phys. Chem. Chem. Phys.* **11** 3805–21

[23] Amendola V, Osman M B and Stellacci F 2010 A study of the surface plasmon resonance of silver nanoparticles by the discrete dipole approximation method: effect of shape, size, structure, and assembly *Plasmonics* **5** 85–97

[24] Giuseppe C, Alessandro A S and Orazio P 2002 Ablation of noble metals in liquids: a method to obtain nanoparticles in a thin polymeric film *Phys. Chem. Chem. Phys.* **4** 2787–91

[25] Emilia G, Muniz-Miranda M, Marsili P, Scarpellini D and Giammanco F 2012 Stable gold nanoparticles obtained in pure acetone by laser ablation with different wavelengths *J. Nanopart. Res.* **14** 648

[26] Boyer P, Ménard D and Meunier M 2010 Nanoclustered Co–Au particles fabricated by femtosecond laser fragmentation in liquids *J. Phys. Chem.* C **114** 13497–500

[27] Santillán J M J, Videla F A, Fernández van Raap M B, Schinca D C and Scaffardi L B 2012 Size dependent Cu dielectric function for plasmon spectroscopy: characterization of colloidal suspension generated by fs laser ablation *J. Appl. Phys.* **112** 054319

[28] Stratakis E 2012 Nanomaterials by ultrafast laser processing of surfaces *Sci. Adv. Mater.* **4** 407–31

[29] Axente E, Noël S, Hermann J, Sentis M and Mihailescu I N 2009 Subpicosecond laser ablation of copper and fused silica: initiation threshold and plasma expansion *Appl. Surf. Sci.* **255** 9734–7

[30] Gamaly E G, Madsen N R, Duering M, Rode A V, Kolev V Z and Luther-Davies B 2005 Ablation of metals with picosecond laser pulses: evidence of long-lived nonequilibrium conditions at the surface *Phy. Rev.* B. **71** 174405

[31] Bärsch N, Jakobi J, Weiler S and Barcikowski S 2009 Pure colloidal metal and ceramic nanoparticles from high-power picosecond laser ablation in water and acetone *Nanotechnology* **20** 445603

[32] Hermann J, Noël S, Itina T E, Axente E and Povarnitsyn M E 2008 Correlation between ablation efficiency and nanoparticle generation during the short-pulse laser ablation of metals *Laser Phys.* **18** 374–9

[33] Barcikowski S, Menéndez-Manjón A, Boris C, Marijus B and Gediminas R 2007 Generation of nanoparticle colloids by picosecond and femtosecond laser ablations in liquid flow *Appl. Phys. Lett.* **91** 083113

[34] Riabinina D, Mohamed C and Margot J 2012 Dependence of gold nanoparticle production on pulse duration by laser ablation in liquid media *Nanotechnology* **23** 135603

[35] Hamad S, Gopala Krishna P, Sreedhar S, Tewari S P and Venugopal Rao S 2012 Femtosecond and picosecond ablation of aluminum for synthesis of nanoparticles and nanostructures and their optical characterization *Proc. SPIE* **8245** 82450L

[36] Gopala Krishna P, Hamad S, Sreedhar S, Tewari S P and Venugopal Rao S 2012 Fabrication and characterization of aluminum nanostructures and nanoparticles obtained using femtosecond ablation technique *Chem. Phys. Lett.* **530** 93–7

[37] Menendez-Manjon A, Wagener P and Barcikowski S 2011 Transfer-matrix method for efficient ablation by pulsed laser ablation and nanoparticle generation in liquids *J. Phys. Chem.* C **115** 5108–14

[38] Tilaki R M, Iraji Zad A and Mahdavi S M 2006 Stability, size and optical properties of silver nanoparticles prepared by laser ablation in different carrier media *Appl. Phys.* A **84** 215–9

[39] Yan Z, Compagnini G, and Chrisey D B 2010 Generation of AgCl cubes by excimer laser ablation of bulk Ag in aqueous NaCl solutions *J. Phys. Chem.* C **115** 5058–62

[40] Nath A and Khare A 2011 Size induced structural modifications in copper oxide nanoparticles synthesized via laser ablation in liquids *J. Appl. Phys.* **110** 043111

[41] Achord J M and Hussey C L 1980 Determination of dissolved oxygen in nonaqueous electrochemical solvents *Anal. Chem.* **52** 601–2

[42] Miranda M M, Gellini C, Simonelli A, Tiberi M, Giammanco F and Giorgetti E 2013 Characterization of copper nanoparticles obtained by laser ablation in liquids *Appl. Phys.* A **110** 829–33

[43] Miranda M M, Cristina G and Emilia G 2011 Surface-enhanced Raman scattering from copper nanoparticles obtained by laser ablation *J. Phys. Chem.* C **115** 5021–7

[44] Gopala Krishna P, Hamad S, Tewari S P, Sreedhar S, Prasad M D and Venugopal Rao S 2013 Silver nano-entities through ultrafast double ablation in aqueous media for SERS and photonics applications *J. Appl. Phys.* **113** 073106

[45] Nielsen J B, Savolainen J M, Christensen M S and Balling P 2010 Ultra-short pulse laser ablation of metals: threshold fluence, incubation coefficient and ablation rates *Appl. Phys.* A **101** 97–101

[46] Garcia M A 2011 Surface plasmons in metallic nanoparticles: fundamentals and applications *J. Phys. D: Appl. Phys.* **44** 283001

[47] Dickenson R G and Dillon R T 1929 The Raman spectrum of gypsum *Proc. Natl Acad. Sci. USA* **15** 695–9

[48] CAS Data base list, Raman spectra of dichloromethane Chemical Book CAS: 75-09-2

[49] Neelakantan P, Krishnan R S and Iitaka Y 1963 Raman spectrum of C-deuterated γ glycine ($NH_3^+CD_2COO^-$) *Proc. Indian Acad. Sci.* A **58** 275–8

[50] Andrew B, Anthony A and Torrie B 1984 Raman and infrared spectra of crystalline chloroform *Chem. Phys. Lett.* **104** 65–70

[51] Sheik-Bahae M, Said A A and Vanstryland E W 1989 High-sensitivity, single-beam n_2 measurements *Opt. Lett.* **14** 955–7

[52] Yin M, Li H P, Tang S H and Ji W 2000 Determination of nonlinear absorption and refraction by single Z-scan method *Appl. Phys.* B **70** 587–91

[53] Hamad S, Tewari S P, Giribabu L and Venugopal Rao S 2012 Picosecond and femtosecond optical nonlinearities of novel corroles *J. Porph. Phth.* **16** 140–8

[54] Anusha P T, Swain D, Hamad S, Giribabu L, Prashant T S, Tewari S P and Venugopal Rao S 2012 Ultrafast excited state dynamics and third order optical nonlinearities of novel corroles *J. Phys. Chem.* C **116** 17828–37

[55] Venugopal Rao S, Prashant T S, Sarma T, Panda P K, Swain D and Tewari S P 2011 Two-photon and three-photon absorption in dinapthoporphycenes *Chem. Phys. Lett.* **514** 98–103

[56] Swain D, Anusha P T, Sarma T, Panda P K and Venugopal Rao S 2013 Dispersion studies of optical nonlinearity and excited state dynamics in cyclo[4]naphthobipyrroles *Chem. Phys. Lett.* **580** 73–7

[57] Sarma T, Panda P K, Anusha P T and Venugopal Rao S 2011 Dinapthoporphycenes: synthesis and nonlinear optical properties *Org. Lett.* **13** 188–91

[58] Nag A, Kumar A, Kiran P P, Chakraborty S, Kumar G R and Sarma D D 2008 Optically bi-functional hetero-Structured nanocrystals *J. Phys. Chem.* C **112** 8229–33

[59] Kiran P P, Bhaktha B N S, Narayana Rao D and De G 2004 Nonlinear optical properties and surface-plasmon enhanced optical limiting in Ag–Cu nanoclusters co-doped in SiO_2 sol–gel films *J. Appl. Phys.* **96** 6717–23

[60] Sreeja R, Reshmi R, Aneesh P M and Jayaraj M K 2012 Liquid phase pulsed laser ablation of metal nanoparticles for nonlinear optical applications *Sci. Adv. Mater.* **4** 439–48

[61] Philip R, Kumar G R, Sandhyarani N and Pradeep T 2000 Picosecond optical nonlinearity in monolayer-protected gold, silver, and gold–silver alloy nanoclusters *Phys. Rev.* B **62** 13160–6

[62] Srinivas N K M N, Venugopal Rao S and Narayana Rao D 2003 Saturable and reverse saturable absorption of rhodamine B in methanol and water *J. Opt. Soc. Am.* B **20** 2470–9

[63] Venkatram N, Narayana Rao D, Giribabu L and Venugopal Rao S 2008 Femtosecond nonlinear optical properties of alkoxy phthalocyanines at 800 nm studied using Z-Scan technique *Chem. Phys. Lett.* **464** 211–5

[64] Sheik-Bahae M, Said A A, Wei T H and Hagan D J 1999 Sensitive measurement of optical nonlinearities using a single beam *IEEE J. Quantum Electron.* **26** 760–9

[65] Fujiwara H, Yanagida S and Kamat P V 1999 Visible laser induced fusion and fragmentation of thionicotinamide-capped gold nanoparticles *J. Phys. Chem.* C **103** 2589–91

[66] Link S, Burda C, Mohamed M B, Nikoobakht B and El-Sayed M A 1999 Laser photothermal melting and fragmentation of gold nanorods: energy and laser pulse-width dependence *J. Phys. Chem.* A **103** 1165–70

[67] Besner S, Kabashin A V and Meunier M 2006 Fragmentation of colloidal nanoparticles by femtosecond laser-induced supercontinuum generation *Appl. Phys. Lett.* **89** 233122

[68] Amendola V, Dini D, Polizzi S, Shen J, Kadish K M, Mario J F C, Hanack M and Meneghetti M 2009 Self-healing of gold nanoparticles in the presence of zinc phthalocyanines and their very efficient nonlinear absorption performances *J. Phys. Chem.* C **113** 8688–95

[69] Torres-Torres C, Reyes-Esqueda J A, Cheang-Wong J C, Crespo-Sosa A, Rodríguez-Fernández L and Oliver A 2008 Optical third-order nonlinearity by nanosecond and picosecond pulses in Cu nanoparticles in ion-implanted silica *J. Appl. Phys.* **104** 014306

[70] Gomez L A, dos Santos F E, Gomes A S L, de Araújo C B, Kassab L R P and Hora W G 2008 Near-infrared third-order nonlinearity of PbO–GeO_2 films containing Cu and Cu_2O nanoparticles *Appl. Phys. Lett.* **92** 141916

[71] Takeda Y, Plaksin O A, Kono K and Kishimoto N 2005 Nonlinear optical properties of Cu nanoparticles in various insulators fabricated by negative ion implantation *Surf. Coat. Technol.* **196** 30–3

[72] Wang Y H, Wang Y M, Lu J D, Ji L L, Zang R G and Wang R W 2010 Nonlinear optical properties of Cu nanoclusters by ion implantation in silicate glass *Opt. Commun.* **283** 486–9

[73] Tanahashi I, Hideyuki I, Koichiro T and Mito A 1999 Preparation and femtosecond third-order nonlinear optical properties of Cu/SiO_2 composite thin films *Japan. J. Appl. Phys.* **38** 5079–82

[74] Aleksandr R, Bruno P, Debrus S, Rashid G, Stepanov A, Nurdogan C, Buchal C and Sibel U 2005 Nonlinear optical absorption of ZnO doped with copper nanoparticles in the picosecond and nanosecond pulse laser field *Appl. Opt.* **44** 2839–45

[75] Ganeev R A, Ryasnyanskii A I, Stepanov A L, Kondirov M K and Usmanov T 2003 Nonlinear properties of composites based on dielectric layers containing copper and silver nanoparticles *Opt. Spectrosc.* **95** 967–75

[76] Guanjun Y, Peng Z, Dong Z, Zhang C, Liangyao C and Qian S 2007 Ultrafast third-order nonlinear optical response of Cu : Bi_2O_3 nanocomposite films *Physica* B **393** 188–94

[77] Serna R, Ballesteros J M, Solis J, Afonso C N, Osborne D H, Haglund R F Jr and Petford-Long R F 1998 Laser-induced modification of the nonlinear optical response of laser-deposited Cu : Al_2O_3 nanocomposite films *Thin Solid films* **318** 96–9

[78] Ballesteros J M, Serna R, Solis J, Afonso C N, Petford-Long A K, Osborne D H and Haglund R F Jr 1997 Pulsed laser deposition of Cu : Al_2O_3 nanocrystal thin films with high third-order optical susceptibility *Appl. Phys. Lett.* **71** 2445–7

[79] del Coso R and Solis J 2004 Relation between nonlinear refractive index and third-order susceptibilities of absorbing media *J. Opt. Soc. Am.* B **21** 640–4

[80] Ganeev R A, Ryasnyansky A I, Kamalov Sh R, Kodirov M K and Usmanov T 2001 Nonlinear susceptibilities, absorption coefficients and refractive indices of colloidal metals *J. Phys. D: Appl. Phys.* **34** 1602–11

[81] Yan Z, Bao R, Dinu C Z, Huang Y, Caruso A N and Chrisey D B 2010 Laser ablation induced agglomeration of Cu nanoparticles in sodium dodecyl sulfate aqueous solution *J. Optoelectron. Adv. Mater.* **12** 437–9

[82] Werner D, Hashimoto S, Tomita T, Matsuo S and Makita Y 2008 In situ spectroscopic measurements of laser ablation induced splitting and agglomeration of metal nanoparticles in solution *J. Phys. Chem.* C **112** 16801–8